One-Step Image Reconstruction for Cine MRI with a Quadratic Constraint

Gengsheng L. Zeng[1,2]*, Xiaodong Ma[2], and Chun Yuan[2]

[1]*Utah Valley University, Orem, UT, United States.*

[2]*University of Utah, Salt Lake City, UT, United States.*

***Correspondence:**
Larry Zeng, Ph.D., Professor of Computer Science, Utah Valley University, USA.

Received: 02 May 2024; **Accepted:** 07 Jun 2024; **Published:** 16 Jun 2024

ABSTRACT

Motivation: *In cine MRI, the measurements within each timeframe alone are too noisy for image reconstruction. Some information must be 'borrowed' from other time frames and the reconstruction algorithm is a slow iterative procedure.*

Goals: *We set up a constrained objective function, which uses the measurements at other time frames to regularize the image reconstruction. We derive a non-iterative algorithm to minimize this objective function.*

Approach: *The derivation of the algorithm is based on the calculus of variations. The resultant algorithm is in the form of filtered backprojection.*

Results: *The feasibility of the proposed algorithm is demonstrated with a clinical patient brain study.*

Impact: *Non-iterative reconstruction that minimizes a constrained objective function significantly increases the throughput in healthcare institutions. This may translate to reduced healthcare costs. The new reconstruction formula has a closed form that gives an explicit expression of how to incorporate the reference image in dynamic reconstruction.*

Keyword
Cine MRI, Image reconstruction.

Introduction
Cine MRI provides detailed information on both anatomy changes and dynamic motion within a patient. It requires very fast data acquisition that contains enough information to reconstruct the entire image [1-4]. At each time frame, the k-space may not be fully sampled, and the measurements may be noisy.

Some image information changes fast from one time frame to another, while some other image information changes slowly. Therefore, some image information can be 'borrowed' from neighboring time frame to assisting image reconstruction at the current time frame, so that this reconstructed image is not as noisy and does not contain as many artifacts.

Many methods are available to 'borrow' data outside of the current timeframe. One popular method is the use of the low rank constraint [5]. Low-rankness methods commonly explore the linear correlations among multiple MRI images. In other words, the low rankness encourages the different images at different time frames to look like each other. An iterative algorithm is required to minimize the objective function that contains a rank term. For example, the alternating direction methods of multipliers (ADMM) framework is commonly used to solve the minimization problem [6].

Another group of cine MRI reconstruction methods is based on the compressed sensing framework [7-11]. Compressed sensing problems are solved by iterative algorithms and their associated objective functions commonly use the L_1 norm or the L_0 norm [12,13].

In this paper, we propose an image domain denoising method by 'borrowing' image information from other timeframes [14]. The proposed algorithm is non-iterative and has a closed-form formula, similar to [9]. Thus, the proposed method is computationally efficient.

Methods
Algorithm Derivation
We consider the following objective function v to be minimized:

$$v(f) = \left\| [Rf](s,\vec{\theta}) - p(s,\vec{\theta}) \right\|^2 + \beta \|f - g\|^2, \tag{1}$$

where $f(\vec{x})$ is the three-dimensional (3D) image to be reconstructed, $g(\vec{x})$ is a reference 3D image that $f(\vec{x})$ should somewhat resemble, Rf is the 3D Radon transform of the function $f(\vec{x})$, $p(s,\vec{\theta})$ is a measurement of the Radon transform, and β is a controlling parameter.

Since the 3D Radon transform of the function $f(\vec{x})$ can be expressed as

$$[Rf](s,\vec{\theta}) = \iiint_{\vec{x}} f(\vec{x})\delta(\vec{x}\cdot\vec{\theta} - s)d\vec{x}, \tag{2}$$

Then (1) becomes

$$v(f) = \int_s \iint_{\vec{\theta}} \left[\iiint_{\vec{x}} f(\vec{x})\delta(\vec{x}\cdot\vec{\theta}-s)d\vec{x} - p(s,\vec{\theta}) \right]^2$$

$$d\vec{\theta}ds + \beta \iiint_{\vec{x}} [f(\vec{x}) - g(\vec{x})]^2\, d\vec{x}. \tag{3}$$

The calculus of variations method [15] is used to find the optimal $f(\vec{x})$. The initial step of this method is to replace the function $f(\vec{x})$ in (3) by the sum of two functions $f(\vec{x}) + \varepsilon\eta(\vec{x})$. The next step is to set the partial derivative $\left.\frac{dv}{d\varepsilon}\right|_{\varepsilon=0}$ to zero. That is,

$$0 = 2\int_s \iint_{\vec{\theta}} \left\{ \left[\iiint_{\vec{x}} f(\vec{x})\delta(\vec{x}\cdot\vec{\theta}-s)d\vec{x} - p(s,\vec{\theta}) \right] \times \left[\iiint_{\vec{x}} \eta(\vec{x})\delta(\vec{x}\cdot\vec{\theta}-s)d\vec{x} \right] \right\} d\vec{\theta}ds +$$

$$2\beta \iiint_{\vec{x}} [f(\vec{x}) - g(\vec{x})]\eta(\vec{x})\, d\vec{x}. \tag{4}$$

In practice, the function $f(\vec{x})$ is compact, bounded, and continuous almost everywhere. After changing the order of integrals, we have

$$0 = \iiint_{\vec{x}} \eta(\vec{x}) \times \left\{ \int_s \iint_{\vec{\theta}} \left[\iiint_{\hat{x}} f(\hat{x})\delta(\hat{x}\cdot\vec{\theta}-s)d\hat{x} - p(s,\vec{\theta}) \right] \right.$$

$$\left. \delta(\vec{x}\cdot\vec{\theta}-s)d\vec{\theta}ds + \beta[f(\vec{x}) - g(\vec{x})] \right\} d\vec{x}. \tag{5}$$

Equation (5) is in the form of

$$0 = \iiint_{\vec{x}} \eta(\vec{x})c(\vec{x})d\vec{x}, \tag{6}$$

where $\eta(\vec{x})$ is any arbitrary function. According to the calculus of variations, one must have

$$c(\vec{x}) = 0, \tag{7}$$

which is the Euler-Lagrange equation. The Euler-Lagrange equation in our case is

$$\int_s \iint_{\vec{\theta}} \left[\iiint_{\hat{x}} f(\hat{x})\delta(\hat{x}\cdot\vec{\theta}-s)d\hat{x} - p(s,\vec{\theta}) \right]$$

$$\delta(\vec{x}\cdot\vec{\theta} - s)d\vec{\theta}ds + \beta[f(\vec{x}) - g(\vec{x})] = 0. \tag{8}$$

By rearranging the terms, eq. (8) can be rewritten as

$$\int_s \iint_{\vec{\theta}} \left[\iiint_{\hat{x}} f(\hat{x})\delta(\hat{x}\cdot\vec{\theta}-s)d\hat{x} \right] \delta(\vec{x}\cdot\vec{\theta}-s)d\vec{\theta}ds + \beta f(\vec{x})$$

$$= \int_s \iint_{\vec{\theta}} p(s,\vec{\theta})\delta(\vec{x}\cdot\vec{\theta}-s)d\vec{\theta}ds + \beta g(\vec{x}). \tag{9}$$

Notice that

$$b(\vec{x}) = \int_s \iint_{\vec{\theta}} p(s,\vec{\theta})\delta(\vec{x}\cdot\vec{\theta}-s)d\vec{\theta}ds \tag{10}$$

is the 3D Radon backprojection of the projection data $p(s,\vec{\theta})$. The relationship between $b(\vec{x})$ and $f(\vec{x})$ is that $b(\vec{x})$ is the blurred version of $f(\vec{x})$, and the convolution kernel for this blurring effect is $\frac{1}{\|\vec{x}\|^2}$. In other words,

$$\int_s \iint_{\vec{\theta}} \delta(\hat{x}\cdot\vec{\theta}-s)\delta(\vec{x}\cdot\vec{\theta}-s)d\vec{\theta}ds = \frac{1}{\|\hat{x}-\vec{x}\|^2}, \tag{11}$$

and

$$\iiint_{\hat{x}} f(\hat{x}) \left[\frac{1}{\|\hat{x}-\vec{x}\|^2} + \beta\delta(\hat{x}-\vec{x}) \right] d\hat{x} = b(\vec{x}) + \beta g(\vec{x}). \tag{12}$$

The left-hand-side of (12) is in the form of a 3D convolution. The Fourier domain version of (12) is given as

$$F(\vec{\omega}) \left(\frac{1}{\|\vec{\omega}\|^2} + \beta \right) = B(\vec{\omega}) + \beta G(\vec{\omega}), \tag{13}$$

where the capital letters are used to represent the 3D Fourier transform of their spatial domain counterparts, which are represented in lowercase letters. The frequency domain counterpart of the spatial domain variable $\vec{x}$ is $\vec{\omega}$.

Solving for $F(\vec{\omega})$ from (13), we have

$$F(\vec{\omega}) = \frac{B(\vec{\omega}) + \beta G(\vec{\omega})}{\frac{1}{\|\vec{\omega}\|^2} + \beta} = \|\vec{\omega}\|^2 \frac{B(\vec{\omega}) + \beta G(\vec{\omega})}{1 + \beta\|\vec{\omega}\|^2}. \tag{14}$$

This closed-form expression is the main result of our theoretical derivation.

Let us consider two extreme cases. When $\beta = 0$ (no regularization),

$$F_{\beta=0}(\vec{\omega}) = \|\vec{\omega}\|^2 B(\vec{\omega}), \qquad (15)$$

which is equivalent to the 3D Radon inversion formula [16]. The Laplace operator, $\frac{\partial}{\partial^2 x} + \frac{\partial}{\partial^2 y} + \frac{\partial}{\partial^2 z}$, can be implemented in the Fourier domain as a filter of $\|\vec{\omega}\|^2$. If we change the order of filtering and backprojection in (15), the filter becomes one-dimensional (1D) and is the second order derivative in the spatial (Radon) domain.

When, $\beta \to \infty$ (too much regularization),

$$F_{\beta\to\infty}(\vec{\omega}) = G(\vec{\omega}), \qquad (16)$$

which is equivalent to $f = g$ in the spatial domain. In this extreme case, the measurements are ignored, and the final image is the same as the reference image. When $0 < \beta < \infty$, (14) gives a regularized reconstruction of f. The reference image g can be chosen as the static image reconstructed by using the summation of all the measured k-space data from every cardiac timeframe.

Algorithm Implementation

The proposed one-step regularized cine MRI reconstruction algorithm can be implemented as the following steps.

Step 1: Prepare two images, by a method presented in Section 2.1. One image is reconstructed using the current timeframe data, and the other image is reconstructed using the sum of all timeframe data. The first image $f_{\beta=0}(\vec{x})$ is the 3D inverse Fourier transform of $F_{\beta=0}(\vec{\omega})$, and the second image $f_{\beta\to\infty}(\vec{x})$ is the 3D inverse Fourier transform of $F_{\beta\to\infty}(\vec{\omega})$.

Step 2: Select a parameter β. Combine the two images produced in Step 1 in the Fourier domain as

$$F(\vec{\omega}) = \frac{F_{\beta=0}(\vec{\omega}) + \beta\|\vec{\omega}\|^2 F_{\beta\to\infty}(\vec{\omega})}{1 + \beta\|\vec{\omega}\|^2}. \qquad (17)$$

Step 3: Find the 3D inverse Fourier transform of $F(\vec{\omega})$ obtained from Step 2 and obtain the final image $f(\vec{x})$. In reality, the numerator of (17) can be implemented in the spatial domain, because the second order derivative operation is very easy to implement for the 3D Radon data along one dimension. However, we do not know an easy way to implement the filter $\frac{1}{1+\beta\|\vec{\omega}\|^2}$ in the spatial domain, because the convolution kernel in the spatial domain needs to be numerically evaluated.

Our cine MRI used 3D radial sampling in the k-space, with 3D golden-angle radial (Koosh ball) trajectories. Some imaging parameters are as follows: the number of readouts (Nkx) was 480, the number of spokes was 3489 in one cardiac cycle, and the image matrix size was 240 x 240 x 240. The data was grouped into 16 timeframes in a cardiac cycle. We used 20 coils for parallel imaging. However, only one coil was used in this study to illustrate the effectiveness of the proposed methodology.

The proposed image reconstruction method is based on a revision of the standard 3D Radon inversion formula. After the 1D inverse Fourier transform along the radial lines, each datapoint in the spatial domain represents a 2D planar integral of the object. The kooshball-like spoke measurement geometry makes the planar integral measurements have a density function of $1/r^2$, where r is the distance from the datapoint location to the coordinate origin. This non-uniform $1/r^2$ effect is compensated for by the 1D Laplacian operator performed in each radial direction. The Jacobian factor in the formula accounts for the sample distribution on the spheres centered at the k-space origin. For the golden-angle radial sampling scheme, the spokes are fairly uniformly distributed. Therefore, the Jacobian factor can be approximated as unity [17,18].

Results

Cine MRI data acquired from Coil #1 was chosen in this paper to illustrate the proposed algorithm. Results at timeframes #1, #8, and #16 in a cardiac cycle are shown in this section. The patient's head did not move during the cardiac cycles; however, the beating heart caused the blood vessel pulsation.

At timeframe #1, reconstructed images of slice #120 at x, y, and z direction are displayed in Figures 1, 2, and 3, respectively. Three different cases are shown for each orientation: $\beta = 0.0$; $\beta = 0.0005$; $\beta = 500$.

Similarly, at timeframe #8, reconstructed images of slice #120 at x, y, and z direction are displayed in Figures 4, 5, and 6, respectively. At timeframe #16, reconstructed images of slice #120 at x, y, and z direction are displayed in Figures 7, 8, and 9, respectively.
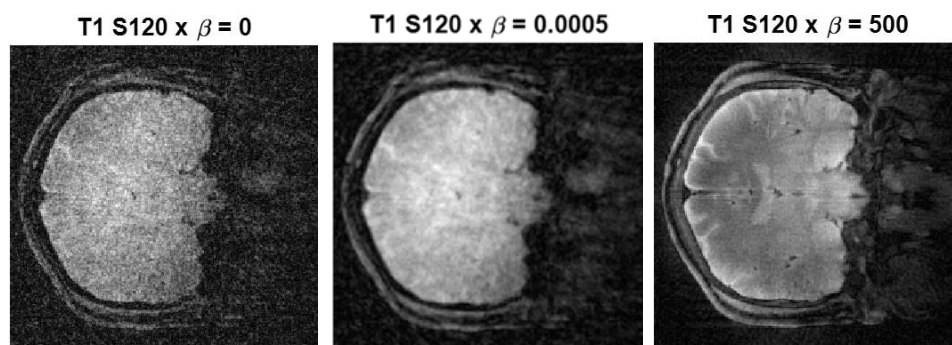

Figure 1: Reconstruction images of slice $x = 120$ at timeframe #1 using three β values: 0, 0.0005, and 500.
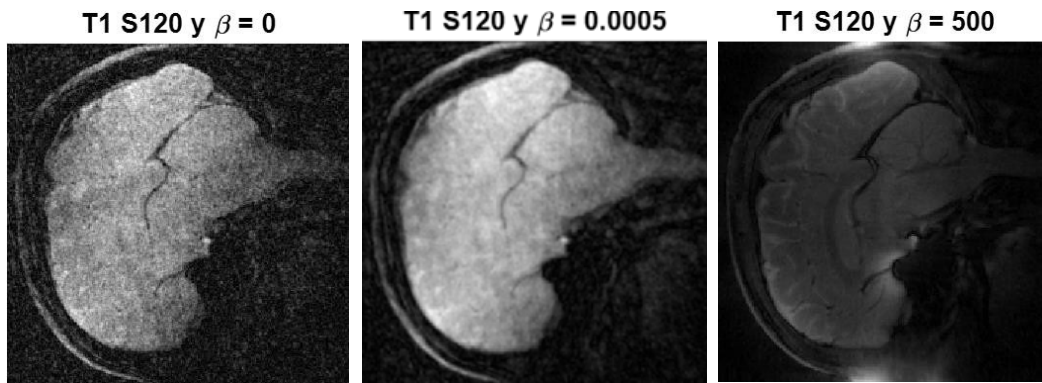
T1 S120 y $\beta = 0$ **T1 S120 y $\beta = 0.0005$** **T1 S120 y $\beta = 500$**

Figure 2: Reconstruction images of slice $y = 120$ at timeframe #1 using three β values: 0, 0.0005, and 500.

T1 S120 z $\beta = 0$ **T1 S120 z $\beta = 0.0005$** **T1 S120 z $\beta = 500$**
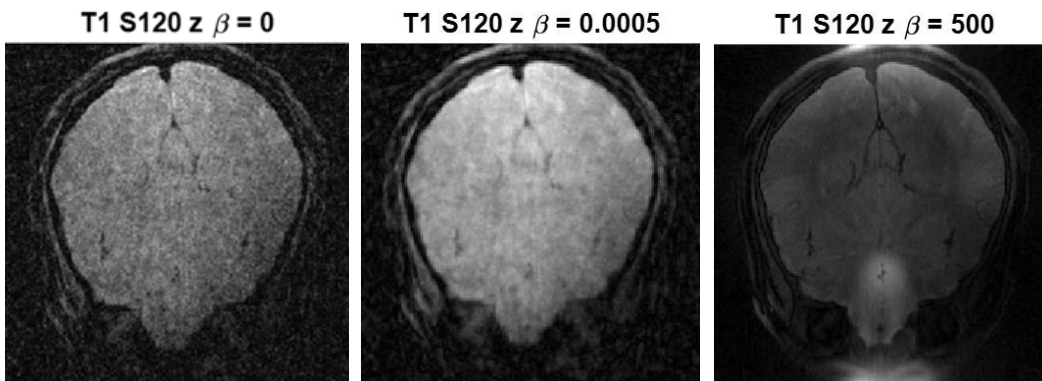
Figure 3: Reconstruction images of slice $z = 120$ at timeframe #1 using three β values: 0, 0.0005, and 500.

T8 S120 x $\beta = 0$ **T8 S120 x $\beta = 0.0005$** **T8 S120 x $\beta = 500$**
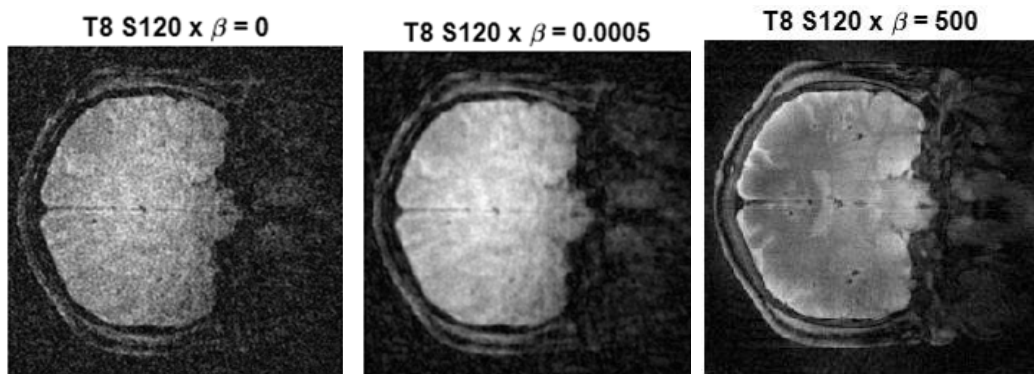
Figure 4: Reconstruction images of slice $x = 120$ at timeframe #8 using three β values: 0, 0.0005, and 500.

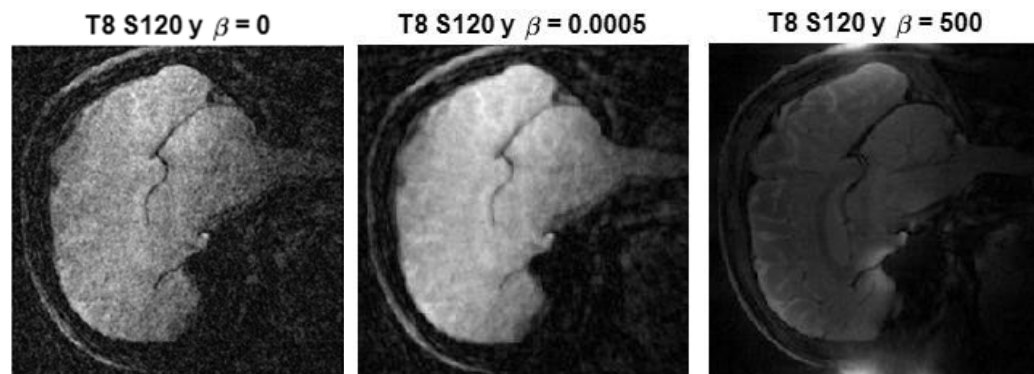**T8 S120 y $\beta = 0$** **T8 S120 y $\beta = 0.0005$** **T8 S120 y $\beta = 500$**

Figure 5: Reconstruction images of slice $y = 120$ at timeframe #8 using three β values: 0, 0.0005, and 500.

Figure 6: Reconstruction images of slice z = 120 at timeframe #8 using three β values: 0, 0.0005, and 500.
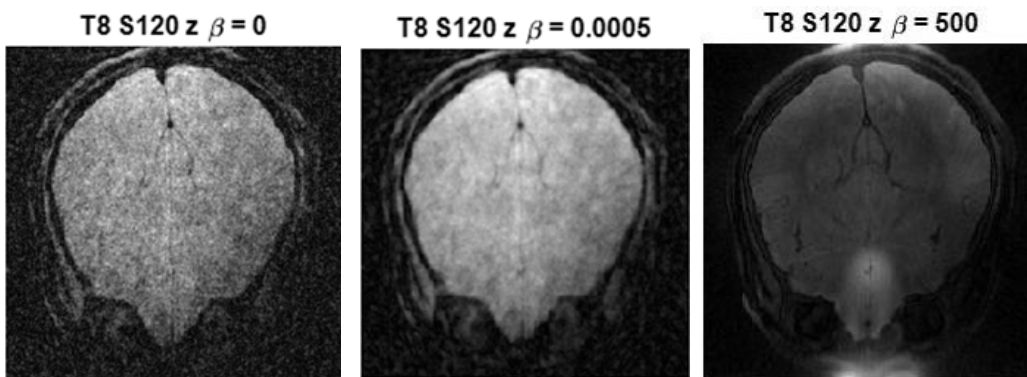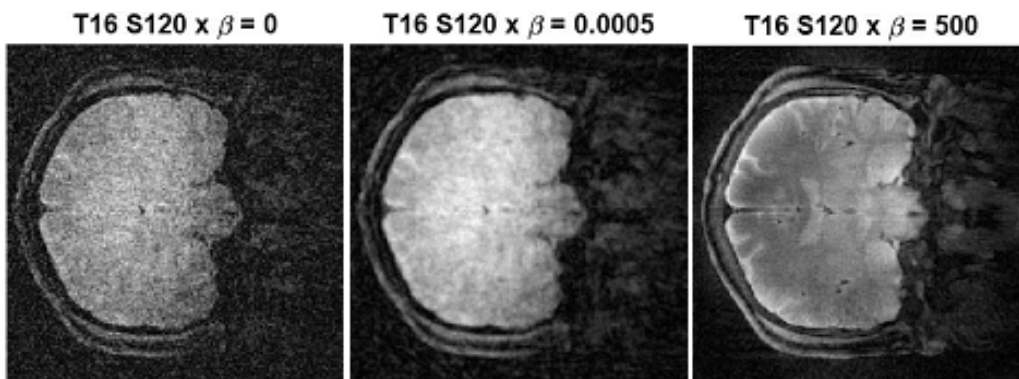

Figure 7: Reconstruction images of slice x = 120 at timeframe #16 using three β values: 0, 0.0005, and 500.
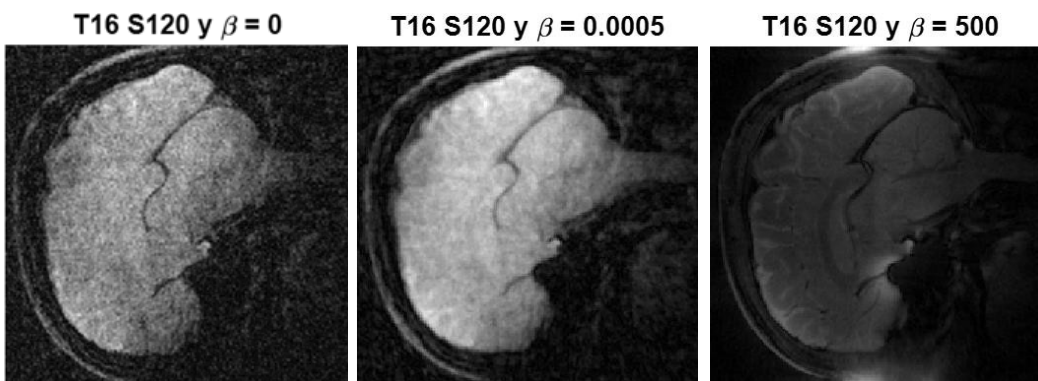

Figure 8: Reconstruction images of slice y = 120 at timeframe #16 using three β values: 0, 0.0005, and 500.
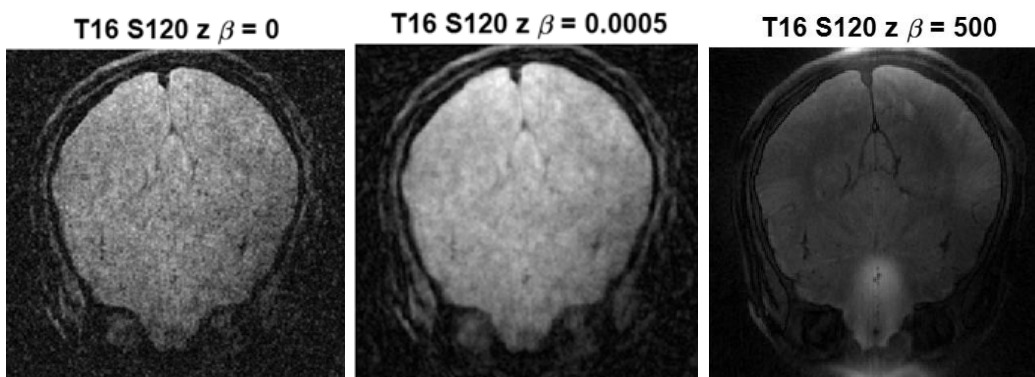

Figure 9: Reconstruction images of slice z = 120 at timeframe #16 using three β values: 0, 0.0005, and 500.

The reconstructed images with $\beta = 0$ carry the correct information, but unfortunately, they are very noisy. It is observed that the images with $\beta = 500$ are least noisy, but they are wrong images because they do not contain much dynamic information. Images with large β values have too much influence from the static reference image. A small β value such as 0.0005 seems to be a proper choice.

Conclusion

Due to the nature of cine MRI, the acquisition time is short, the k-space is sparsely sampled, and the signal- to-noise ratio is low. To improve signal-to-noise ratio, a constrained objective function is set up that provides a reference image. This objective function is in a quadratic form. A quadratic objective function does not automatically translate into an efficient analytic algorithm due to the huge size of the imaging matrix that cannot be directly stored and inverted.

This paper develops an analytic method to find the optimal solution of a quadratic objective function. This algorithm is expressed in the Fourier domain, and the inversion of a huge imaging matrix is avoided. This optimal solution of the optimization problem is not a simple linear combination of the current timeframe image and the average timeframe image. The combination of these two images depends on the frequency.

The parameter β defined in the objective function should be small enough not to let the reference image dominate the reconstruction, and large enough to fill in some missing information that the primary data lacks. Unfortunately, there is no explicit formula to determine β. Trial-and-error experiments may be needed to select a satisfactory value of β.

References

1. Menchón-Lara RM, Simmross-Wattenberg F, Casaseca-de-la-Higuera P, et al. Reconstruction techniques for cardiac cine MRI. Insights Imaging. 2019; 10: 100.

2. Wang X, Uecker M, Feng L. Fast real-time cardiac MRI: A review of current techniques and future directions. Investig Magn Reson Imaging. 2021; 25: 252-265.

3. Hunold P, Maderwald S, Ladd ME, et al. Parallel acquisition techniques in cardiac cine magnetic resonance imaging using TrueFISP sequences: Comparison of image quality and artifacts. J Magn Reson Imaging. 2004; 20: 506-511.

4. Wintersperger BJ, Reeder SB, Nikolaou K, et al. Cardiac CINE MR imaging with a 32-channel cardiac coil and parallel imaging: Impact of acceleration factors on image quality and volumetric accuracy. J Magn Reson Imaging. 2006; 23: 222-227.

5. Miao X, Lingala SG, Guo Y, et al. Accelerated cardiac cine MRI using locally low rank and finite difference constraints. Magn Reson Imaging. 2016; 34: 707-714.

6. Ding Y, Li P, Xiao Y, et al. Efficient dual ADMMs for sparse compressive sensing MRI reconstruction. Math Meth Oper Res. 2003; 97: 207-231.

7. Lustig M, Santos JM, Donoho DL, et al. kt SPARSE: high frame rate dynamic MRI exploiting spatio-temporal sparsity. Proc Intl Soc Mag Reson Med. 2006; 14: 2420.

8. Lustig M, Donoho DL, Pauly JM. Sparse MRI: the application of compressed sensing for rapid MR imaging. Magn Reson Med. 2007; 58: 1182-1195.

9. Zeng GL, Li Y, DiBella ERV. Non-iterative reconstruction with a prior for undersampled radial MRI data. Int J Imag Sys Tech. 2013; 23: 53-58.

10. Huang F, Akao J, Vijayakumar S, et al. k-t GRAPPA: a k-space implementation for dynamic MRI with high reduction factor. Magn Reson Med. 2005; 54: 1172-1184.

11. Tolouee A, Alirezaie J, Babyn P. Compressed sensing reconstruction of cardiac cine MRI using golden angle spiral trajectories. J Magn Reson. 2015; 260: 10-19.

12. Pokala PS, Seelamantula CS. Accelerated weighted l1-minimization for MRI reconstruction under tight frames in complex domain. International Conference on Signal Processing and Communications. 2020; 1-5.

13. Trzasko J, Manduca A. Highly undersampled magnetic resonance image reconstruction via homotopic l0 – minimization. IEEE Trans Med Imaging. 2009; 28: 106-121.

14. Adluru G, McGann C, Speier P, et al. Acquisition and reconstruction of undersampled radial data for myocardial perfusion magnetic resonance imaging. J Magn Reson Imaging. 2009; 29: 466-473.

15. Gelfand IM, Silverman RA. Calculus of variations. Courier Corporation. 2000.

16. Zeng GL. Medical image reconstruction: A conceptual tutorial. Higher Education Press/Springer. 2009.

17. Chan RW, Ramsay EA, Cunningham CH, et al. Temporal stability of adaptive 3D radial MRI using multidimensional golden means. Magn Reson Med. 2009; 61: 354-363.

18. Feng L. Golden-angle radial MRI: Basics, advances, and applications. J Magn Reson Imaging. 2022; 2: 45-62.